MNRAS 000, 1–?? (2016) Preprint 22 August 2016 Compiled using MNRAS LATEX style file v3.0

Abundance stratification in Type Ia supernovae - V. SN 1986G bridging the gap between normal and subluminous SNe Ia

C.Ashall[1]⋆, P.A. Mazzali[1,2], E.Pian[3,4], P.A.James[1]
[1]*Astrophysics Research Institute, Liverpool John Moores University, IC2, Liverpool Science Park, 146 Brownlow Hill, Liverpool L3 5RF, UK*
[2]*Max-Planck-Institut für Astrophysik, Karl-Schwarzschild-Str. 1, D-85748 Garching, Germany*
[3]*Institute of Space Astrophysics and Cosmic Physics, via P. Gobetti 101, I-40129 Bologna, Italy*
[4]*Scuola Normale Superiore, Piazza dei Cavalieri 7, I-56126 Pisa, Italy*

July 2016

ABSTRACT

A detailed spectroscopic analysis of SN 1986G has been performed. SN 1986G 'bridges the gap' between normal and sub luminous type Ia supernova (SNe Ia). The abundance tomography technique is used to determine the abundance distribution of the elements in the ejecta. SN 1986G was found to be a low energy Chandrasekhar mass explosion. Its kinetic energy was 70% of the standard W7 model (0.9×10^{51} erg). Oxygen dominates the ejecta from the outermost layers down to $\sim 9000\,\mathrm{kms}^{-1}$, intermediate mass elements (IME) dominate from $\sim 9000\,\mathrm{kms}^{-1}$ to $\sim 3500\,\mathrm{kms}^{-1}$ with Ni and Fe dominating the inner layers $<\sim 3500\,\mathrm{kms}^{-1}$. The final masses of the main elements in the ejecta were found to be, O=0.33 $M_\odot$, IME=0.69 $M_\odot$, stable NSE=0.21 $M_\odot$, ^{56}Ni=0.14 $M_\odot$. An upper limit of the carbon mass is set at C=0.02 $M_\odot$. The spectra of SN 1986G consist of almost exclusively singly ionised species. SN 1986G can be thought of as a low luminosity extension of the main population of SN Ia, with a large deflagration phase that produced more IMEs than a standard SN Ia.

Key words: supernova: general-supernovae: individual (SN 1986G) - techniques: spectroscopic

1 INTRODUCTION

Type Ia Supernovae (SNe Ia) are predicted to originate from the thermonuclear explosion of a C+O white dwarf (WD) approaching the Chandrasekhar mass limit, but their exact nature remains unclear. There are currently two leading progenitor scenarios, the single degenerate scenario (SDS) and the double degenerate scenario (DDS). In the SDS a C+O WD accretes material from a non-electron-degnerate companion star. When the mass of the C+O WD approaches the Chandrasekhar mass thermonuclear runaway begins, hence a SN Ia is produced (Nomoto et al. 1997). In the DDS two WDs merge, after losing angular momentum in the form of gravitational waves, and explode (Iben & Tutukov 1984). Additional scenarios include the Sub-Chandrasekhar mass explosion of a C+O WD which accretes Helium from a companion (Livne & Arnett 1995), and the collision of two C+O WDs in a triple system, which can detonate following a head-on collision (Rosswog et al. 2009).

Historically it was thought that SNe Ia could be used as standard candles. However, as with much of observational astronomy, when the sample of data increased it soon became apparent that they are a far more diverse group (Phillips et al. 1987, 1992; Leibundgut et al. 1993; Ashall et al. 2016). Normal SNe Ia show a strong correlation between their light curve shape, $\Delta M_{15}(B)$, and absolute magnitude. This correlation is one of the underlying foundations of SN Ia cosmology (Phillips 1993; Phillips et al. 1999). There are, however, a number of subsets of SNe Ia which are less common. Among these, SN 1991bg, after which a subset of SNe Ia are named, was a less luminous explosion which was dominated by intermediate mass elements and showed a rapidly declining light curve. Theoretically SN 1991bg has been interpreted to be the merger of two WDs (Mazzali & Hachinger 2012), but others have suggested a delayed detonation mechanism (Höflich et al. 2002).

SN 1986G was the first object to lead to the question-

⋆ E-mail:c.ashall@2013.ljmu.ac.uk

ing of Type Ia Supernovae (SNe Ia) as standard candles (Phillips et al. 1987). Its light curve (LC) was faster and dimmer than all of the previously discovered SNe Ia. It had a rapidly declining light curve at early phases and slow expansion velocities compared to a normal SNe Ia (Phillips et al. 1987; Cristiani et al. 1992). SN 1986G was located in NGC 5128, also known as Centauras A, which is at a distance 3.42±0.18 Mpc (Ferrarese et al. 2007). This made it one of the closest SNe Ia ever discovered, until SN 2014J (Ashall et al. 2014). SN 1986G was observationally red, with a $(B-V)_{Bmax}$=0.88±0.03 mag. This could be interpreted as SN 1986G suffering form a large amount of extinction. However, SNe Ia suffer from a colour/extinction degeneracy. Recently, for normal SNe Ia, this colour/extinction degeneracy has been overcome (Sasdelli et al. 2016). For unusual SNe Ia this degeneracy still remains an issue, and values of host galaxy extinction can be very uncertain.

SN 1986G is a "transitional" SN Ia. "transitional" in this case refers to SNe Ia that bridge the gap between 91bg-like and normal SNe Ia (Ashall et al. 2016). Figure 1 presents the *B*-band absolute magnitude light curves of four SNe Ia with a variety of decline rates, $\Delta M_{15}(B)$ (2011fe, 2004eo, 1986G and 2005bl). SN 2011fe was a stereotypical normal SNe Ia with $\Delta M_{15}(B)$=1.1±0.05 mag, a broad LC shape, and a normal spectrum, see Figure 2. SN 2004eo had $\Delta M_{15}(B)$=1.47±0.07 mag, it was slightly less luminous than SN 2011fe, and had normal spectra. SN 1986G had $\Delta M_{15}(B)$=1.81±0.07 mag, a narrow LC and a cooler spectrum. SN 2005bl was a 91bg-like SN, with $\Delta M_{15}(B)$=1.93±0.1 mag. SN 1986G sits half-way between normal and subluminous SNe Ia.

The environment of SN 1986G is highly unusual and merits some discussion. The host system is the peculiar radio galaxy NGC 5128 which is generally classified in terms of its optical morphology as a lenticular or elliptical galaxy. This implies a dominant old stellar population, but this may well be misleading, as SN 1986G occurred in the middle of the strong dust lane which gives NGC 5128 its peculiar appearance, but well offset from the active galactic nucleus. The dust lane is generally considered to be the result of a merger with a smaller gas-rich galaxy (Baade & Minkowski 1954; Tubbs 1980), and it is associated with substantial ongoing star formation, which is indicated by strong, extended clumpy Hα emission throughout most of the dust lane (see e.g., Bland et al. 1987). Anderson et al. (2015) found the location of SN 1986G to be associated with detectable Hα emission, even though it is not coincident with a bright H II region, so there is clearly a young stellar population in the immediate vicinity. Transitional SNe Ia are often found in peculiar galaxy environments, and this is clearly the case with SN 1986G.

Figure 2 shows the spectroscopic difference between these SNe Ia. All spectra have been corrected for host galaxy extinction. A strong ~4450 Å Ti II feature is an indicator of a subluminous SN Ia. SN 1986G is one of the few SNe Ia with an intermediate strength Ti II feature. Furthermore, the ratio of the Si II features (~5970 Å and 6355 Å) is a good temperature indicator. (Nugent et al. 1995; Hachinger et al. 2006). It is however an indirect temperature indicator, as it results from the saturation of the Si II λ 6355 line. Si II becomes more abundant with respect to Si III at lower luminosities and temperatures, so that the Si II λ5970 line becomes stronger with respect to the Si λ6355 line. SN 1986G had a larger Si II ratio compared to normal SNe Ia, but one not as strong as a 91bg-like SN Ia. Therefore it is a transitional object. SN 1986G is the only published SNe Ia with these properties and good observational data, which demonstrates that these objects must be rare. SN 2011iv may also be classified as a transitional SN because of its rapidly evolving LC, but it was spectroscopically normal (Foley et al. 2012).

A detailed theoretical understanding of SN 1986G should help to determine the relationship between 91bg-like and normal SNe Ia. This can be done by examining a time series of spectra and analysing their evolution. Normal SNe Ia show properties that are matched by delayed detonation (DD) explosions, and can be modelled using the W7 density profile, which is similar to most DD models except in the outermost layers (Stehle et al. 2005; Mazzali et al. 2008; Ashall et al. 2014). SN 1991bg had a low central density (Mazzali & Hachinger 2012), which favours a merger scenario in which the combined mass of the merging WDs is below the Chandrasekhar mass. Similarly, the density distribution in SN 2003hv, which had $\Delta M_{15}(B)$=1.61 mag, indicates a Sub-Chandrasekhar mass (Mazzali et al. 2011). Subluminous SNe Ia tend to occur in old stellar populations and are at the end of the SNe Ia parameter space (Ashall et al. 2016). Therefore, as it has been shown that 91-bg-like SNe Ia could be the result of a different progenitors/explosion mechanism than normal SNe Ia, the question is at which point do SNe Ia begin to depart from the standard explosion models, and what causes them to be different. The answer may be found by analysing individual transitional SNe Ia in detail. One way to do this is to use the 'abundance tomography' approach (Stehle et al. 2005). This method produces optimally fitting synthetic spectra to match the observed ones, and allows us to infer the abundance distribution in the ejecta. Abundance tomography has been successfully used to model a number of SNe Ia, including SN 2002bo (Stehle et al. 2005), 2003du (Tanaka et al. 2011), 2010jn (Hachinger et al. 2013), 2011fe (Mazzali et al. 2014, 2015), 2014J (Ashall et al. 2014) and 1991T (Sasdelli et al. 2014).

This paper uses the abundance tomography technique to infer the properties of SN 1986G. It starts with a summary of the data used (Section 2), followed by a description of the modelling technique (Section 3). Photospheric-phase models are then presented in Section 4, while Section 5 discusses nebular-phase models. After this the full abundance tomography is carried out (Section 6). In Section 7 the results are re-evaluates and a modified density profile is used to improve the fits. A synthetic light curve is presented in Section 8 and compared to the bolometric light curve of SN 1986G computed from the available photometry. Finally, the results are discussed and conclusions are drawn in Section 9.

2 DATA

Abundance tomography modelling requires a time-series of spectra. The data in this paper come from a variety of sources, which are listed in Table 2. Six spectra published by Cristiani et al. (1992) were used for the photospheric phase models. These spectra cover the range from −3 d to +2 d relative to *B*-band maximum. This is not ideal as it only covers

Table 1. The Δ $M_{15}(B)$ and absolute B band magnitude of the SNe Ia used in Figures 1 and 2.

SN	$\Delta M_{15}(B)$	M_B	References
SN 2011fe	1.1±0.05 mag	-18.99	Munari et al. (2013)
SN 2004eo	1.47±0.07 mag	-18.65	Pastorello et al. (2007)
SN 1986G	1.81±0.07 mag	-17.76	Phillips et al. (1987); Taubenberger et al. (2008)
SN 2005bl	1.93±0.1 mag	-16.45	Taubenberger et al. (2008)

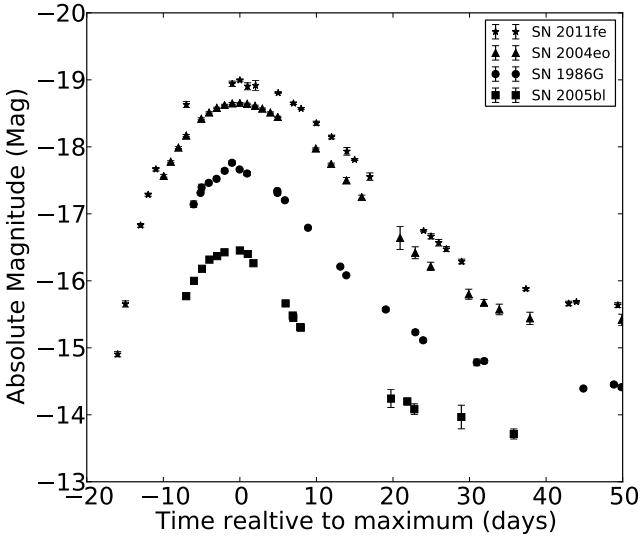

Figure 1. The B band absolute magnitude of four SNe Ia which have a variety of LC shapes.

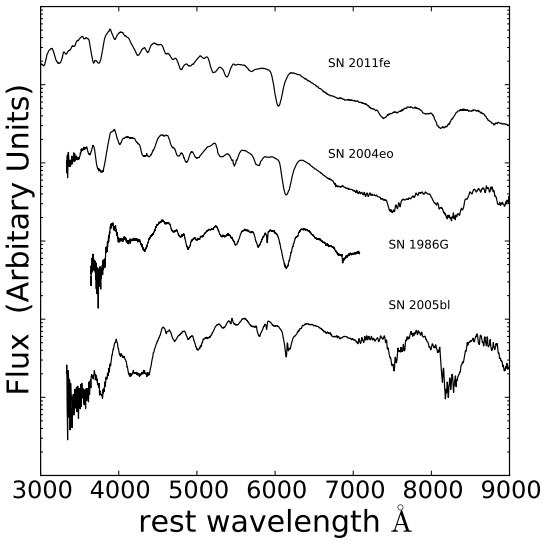

Figure 2. The spectra of four SNe Ia at B band maximum. The SNe correspond to the 4 SNe in Figure 1

a small range in velocity space, but information about the outer (but not the outermost) layers can still be inferred. Two near-UV spectra taken with the International Ultraviolet Explorer (IUE) are also used. Although these spectra have low signal-to-noise, they are important in that they allow us to determine the flux level in the NUV. To probe the inner layers of the SN ejecta a nebular phase spectrum is required. One such spectrum was obtained by Cristiani et al. (1992). The final stage of the modelling process involves modelling the bolometric light curve. The data used to construct the pseudo-bolometric light curve of SN 1986G are taken from a variety of sources (Cristiani et al. 1992; Frogel et al. 1987; Phillips et al. 1987).

Before the spectra can be modelled they must be calibrated in flux. The flux calibration of the spectra was checked by comparing synthetic photometry, obtained from the spectra with the real photometric data. As SN 1986G only has good photometric coverage in two passbands, B and V, flux calibration was checked against the photometry in these filters. If there was a difference in magnitude between the synthetic and observed photometry a linear function was applied to correct the spectra. New synthetic B and V band photometry was then produced and checked against the observed photometry. This process was carried out for all spectra of SN 1986G.

3 MODELLING TECHNIQUES

3.1 Photospheric phase modelling technique

With the objective of carrying out a detailed analysis of the ejecta of SN 1986G, a MC supernova radiative transport code was used to produce synthetic spectra, implementing the 'abundance tomography' method outlined in Stehle et al. (2005). This technique utilises the fact that as time from the SN explosion increases and the SN ejecta expand, deeper and deeper layers can be seen. The ejecta are assume to be in homologous expansion, which can be approximated by the equation $r = v_{ph} \times t_{exp}$, where r is the distance from the centre of the explosion, v_{ph} is the photospheric velocity and t_{exp} is the time from explosion. The code uses the Schuster-Schwarzschild approximation, which assumes that the radiative energy is emitted from an inner boundary as a black body. This approximation is used as it does not require in-depth knowledge of the radiation transport below the optically thick photosphere while still yielding accurate results. The assumption works best when the bulk of the ^{56}Ni is below the photosphere, since ^{56}Ni decay produces the energy which powers the ejecta. At later times significant γ-ray trapping occurs above the photosphere. After bolometric maximum the Schuster-Schwarzschild approximation can cause excess flux in the IR, but since most of the strong

Table 2. The spectra of SN 1986G.

Date	MJD	Phase (days)	source	telescope
7/5/1986	46557	-3	Cristiani et al. (1992)	ESO 2.2m B&C+CCD
7/5/1986	46557	-3	archive.stsci.edu/iue/	International Ultraviolet Explorer
8/5/1986	46558	-2	Cristiani et al. (1992)	ESO 2.2m B&C+CCD
9/5/1986	46558	-2	archive.stsci.edu/iue/	International Ultraviolet Explorer
9/5/1986	46559	-1	Cristiani et al. (1992)	ESO 1.5m B&C+IDS
10/5/1986	46560	+0	Cristiani et al. (1992)	ESO 1.5m B&C+IDS
11/5/1986	46561	+1	Cristiani et al. (1992)	ESO 1.5m B&C+IDS
12/5/1986	46562	+2	Cristiani et al. (1992)	ESO 1.5m B&C+IDS
22/1/1987	46817	+256	Cristiani et al. (1992)	EFOSC 3.6m

lines in a SN Ia are in the UV/Optical (< 6500 Å) this does not affect the results concerning abundances.

The code is a 1D MC radiative transport code (Abbott & Lucy 1985; Mazzali & Lucy 1993; Lucy 1999; Mazzali 2000). It simulates the emission of photon packets at the photosphere. These packets then propagate through the SN atmosphere, where they can undergo Thomson scattering and line absorption. If a packet is absorbed in a line it is re-emitted following a photon branching scheme, which allows both fluorescence (blue to red) and reverse fluorescence (red-to-blue) to occur. This is the process that mostly determined the spectrum of a SN Ia (Mazzali 2000). Electron scattering is a secondary source of opacity in the metal-rich atmosphere of SNe Ia (Pauldrach et al. 1996). Packets which go back into the photosphere are assumed to be re-absorbed. A modified nebular approximation is used to treat the excitation/ionisation state of the gas, to account for NLTE effects caused by the diluted radiation field. The radiation field and the state of the gas are iterated until convergence is achieved. The final spectrum is obtained by computing the formal integral of the radiation field.

The code requires a number of free input parameters, as well as a fixed density profile. A suitable density profile for the explosion must first be chosen. Usually for a SNe Ia the initial density profile used is the W7 profile (Nomoto et al. 1984), which has been shown to produce good results for a range of SNe Ia. The W7 density profile assumes a single-degenerate SN Ia explosion (Nomoto et al. 1984). If W7 does not produce a good fit different density profiles are then tested, such as a Sub-Chandrasekhar (Sub-Ch) mass density profile. The normal process of modelling a time series of spectra involves producing synthetic spectra starting with the earliest epoch. This is done by setting the distance and extinction to the SN, then determining the bolometric luminosity of the ejecta and the photospheric velocity. A typical abundance distribution is then assumed and a synthetic spectrum of the first epoch is produced. Usually 2 or 3 synthetic shells are placed above the photosphere of the first observed spectrum, in order to produce a stratified abundance distribution at higher velocities, and to avoid wrong elements been seen at high velocities in the synthetic spectra. The abundances above the photosphere are varied to produce the best fit to the observed spectrum. Once an acceptable fit is obtained the next spectrum is modelled using the same procedure, and only the abundances inside the previous photosphere are modified. Abundances in the outer layers can affect the synthetic spectra at later epochs. If this is the case iteration is required on the abundances of the elements in the outer layers. Abundances given in this work have an error of ±25%, and photospheric velocities have an error of ±15%. A detail analysis of errors using the 'abundance tomography' method was carried out in the second paper of this series, see Mazzali et al. (2008). The error on the ^{56}Ni mass is ±10%, as it is constrained though multiple methods. For SN 1986G this was done for all of the photospheric phase spectra, up to 2 days past *B*-band maximum.

3.2 Nebular Phase modelling technique

The nebular spectrum was modelled using a 1D NLTE code similar to Mazzali et al. (2007b). The code uses a Monte Carlo scheme to compute the propagation and deposition of the γ-rays and positrons production in the decay of ^{56}Ni to ^{56}Co and ^{56}Fe, based on an assumed density profile, such as W7, and an abundance distribution. In the outer layers the abundances derived in the photospheric phase modelling are used, while inner layers are filled with the abundances that lead to a best match with the observations (Mazzali et al. 2007b). The heating from the energy deposition is balanced by the cooling from line emission. Given a fixed distance and extinction, the mass of synthesised ^{56}Ni in the explosion can be computed. Using a fixed density profile allows the abundance distribution in the inner layers to be determined. The ratio of the strongest [Fe II] and [Fe III] lines is a good indicator of the late time ejecta abundances. This analysis complements the early time spectra, and yields an abundance distribution throughout the whole ejecta.

3.3 Light curve code

A Montecarlo code is used, with a fixed density profile and derived abundance distribution, to compute a synthetic bolometric light curve (Cappellaro et al. 1997; Mazzali et al. 2001). The code computes the emission and propagation of γ-rays and positrons as a function of time, and follows their propagation through the ejecta. When these deposit, optical photons are produces, whose diffusion is also followed with a Montecarlo scheme. The optical opacity is treated with a scheme which is based on the number of effective lines as a function of abundances (Mazzali et al. 2001). This is a good approximation, as line opacity dominates SNe Ia ejecta (Pauldrach et al. 1996).

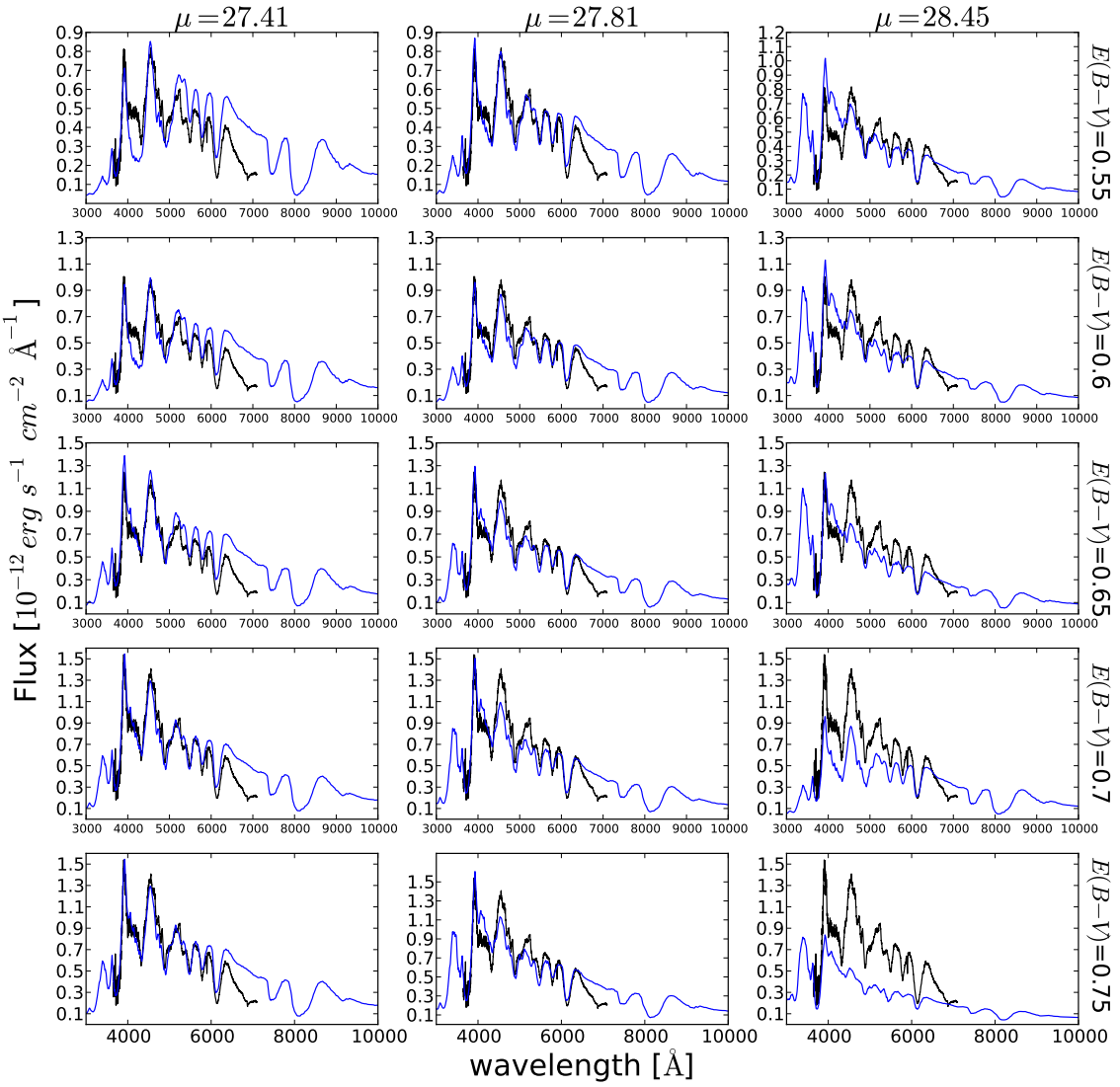

Figure 3. One-zone models of SN 1986G at *B* band maximum, using a variety of distance modulus and extinction values. The observed spectra are in black and the modelled in blue.

4 PHOTOSPHERIC MODELS

4.1 Extinction and distance

The first step in modelling the photospheric spectra of a SN is to set the values for host galaxy extinction and distance. Both of these values are very uncertain for SN 1986G. A range of values have been published for the distance modulus of NGC 5128, ranging from 27.41-28.45 mag (see table 3). A large range of extinction values have also been quoted for SN 1986G, ranging from $E(B-V)_{tot}$=0.6 to 0.9 mag (Nugent et al. 1995; Phillips et al. 1987), as well as $E(B-V)_{tot} = 0.78 \pm 0.07\,mag$ (R_v = 2.4) (Taubenberger et al. 2008). Therefore, we have taken the distance to the SN and host galaxy extinction as free parameters. In our models there is some degeneracy between the distance and the extinction to the SN (Sasdelli et al. 2014). We ran one-zone photospheric phase models on the spectrum at *B* band maximum, with fixed abundances, to determine the most likely range of parameters. Figure 3 shows some of these one-zone models, for a range of distances from table 3. Extinction values range from 0.5 to -0.9 mag and were varied by intervals of 0.05 mag. The range of acceptable values was taken as

Table 3. Published distances to SN 1986G.

Distance modulus (μ)	Method	Source
28.45 ±0.8	Tully Fisher	*a*
27.81±0.2	TRGB	*b*
27.67±0.12	Cepheid	*c*
27.41±0.04	Brightest Stars	*d*

a Richter & Huchtmeier (1984)
b Soria et al. (1996)
c Ferrarese et al. (2007)
d de Vaucouleurs (1980)

$E(B-V)_{tot}$=0.6-0.7 mag [1] and μ = 27.41 − 27.81 mag. For the modelling in this paper we used $E(B-V)_{tot}$ = 0.65 ± 0.5 mag and μ = 27.61 ± 0.4 mag, as these values yield the best fits. The extinction is consistent with that of Nugent et al. (1995). The distance value is in good agreement with the Cepheid distance from Ferrarese et al. (2007), who derive a distance modulus of 27.67±0.12 mag. In the modelling process it is most important to obtain the correct line ratios, line strengths, ionizations and velocities, as these are independent of extinction and yield information about the SN. We find that other values of extinction and distance produce worse fits, even if the abundances are varied.

4.2 Density profiles

Initially, we modelled SN 1986G using two density profiles, W7 and a Sub-Ch mass density profile. The W7 density profile results from a fast deflagration explosion of a Chandrasekhar mass C+O WD. The deflagration wave synthesises 0.5-0.6 $M_{\odot}$ of ^{56}Ni in the inner layers of the star, which is enough to power the light curve of the supernova (Nomoto et al. 1984). This explosion has a kinetic energy $E_{\rm kin}$= 1.3 × 10^{51} erg. The W7 model was selected as SNe 2004eo, 2003du, 2002bo and 2014J can all be reasonably modelled with this density profile and variable amounts of ^{56}Ni. The Sub-Ch mass density profile is an explosion with $E_{\rm kin}$= 1.2 × 10^{51} erg and a total mass of 1.1 $M_{\odot}$ (Shigeyama et al. 1992). It has a larger density at high velocities but contains less mass in the inner part of the ejecta compared to W7.

4.3 Photospheric models

The photospheric phase spectra of SN 1986G are dominated by lines of intermediate mass elements (IME), which is consistent with the low ^{56}Ni mass and rapid LC decline of the SN, and may indicate a stronger deflagration phase. This section discusses the input parameters and the properties of the synthetic spectra at each epoch. Figure 4 presents the synthetic spectra for the photospheric phase of SN 1986G. We adopted for both the W7 and Sub-Ch mass models a rise time to *B* band maximum of 18 days. This is smaller than for normal SNe Ia (e.g., Mazzali et al. 1993), but is typical for a SNe Ia with a fast LC shape. This is because the ejecta of a low-luminosity SN have a smaller opacity and a shorter photon diffusion time as they contain less NSE material (Mazzali et al. 2001). There is very little difference between the two density profiles within the velocity range sampled by the photospheric models (7000-10000 $km\,s^{-1}$). The main differences are in the inner part of the ejecta, which is sampled by nebular phase modelling.

Figure 4 shows the spectral evolution of SN 1986G between 3 days before and 2 days after *B* band maximum. The spectra are dominated by Si II, S II, Fe II, Mg II, Ti II and Cr II lines. Ti II ~4450 Å is not typical of normal SNe Ia, where Ti is normally doubly ionised. Most of the lines from Ti III are however in the UV, <3500 Å.

4.4 -3 days

The top spectrum in Figure 4 was observed 3 days before *B* band maximum. The synthetic spectrum has a photospheric velocity of 10000 km s^{-1}, and bolometric luminosity of 42.55 erg s^{-1}. The converged temperature of the underlying blackbody is 8900 K for the W7 density profile and 9100 K for the Sub-Ch density profile. The effective temperature (T_{eff}) is 8600 K for the W7 density profile and 8700 K for the Sub-Ch density profile. For the W7 density profile the composition is dominated by oxygen (61% by mass), but it also requires some unburnt carbon (2% by mass), IME (Si 26%, S 6%, Ca 2%, Mg 2%), and traces of heavier metals (Ti+Cr 0.36% and Fe 0.15%). Using the Sub-Ch density profile, the synthetic spectrum is dominated by O (52% by mass), with 2% unburnt carbon. IME make up a large fraction of the ejecta (Si 25%, S 15%, Mg 2%, Ca 2%), with the rest consisting of heavier elements (Ti 2%, Cr 2.5%, Fe 0.08%).

4.5 -2 days

The second spectrum in Figure 4 was modelled at 16 days after explosion. There is very little spectral evolution compared to the previous epoch. Using the W7 density profile a photospheric velocity of 9500 kms^{-1} is required, as well as a bolometric luminosity of $\log_{10}$L=42.57 erg s^{-1}. The T_{eff} at this epoch is 8700 K. This spectrum is dominated by oxygen (61%), while IME make up 38% of the elements in this shell (Si 30%, S 6%, Ca, 2%). The Ti, Cr and stable Fe abundances have all increased (Ti+Cr 1.1%, Fe 0.2%), relative to the higher velocity spectrum. This is required as the Ti ~4450 Å feature progressively gets stronger over time. The IUE spectrum has been used to set the flux level in the UV and to constrain the Cr abundance.

The Sub-Ch density profile produces slightly different results. The effective temperature at this epoch is 9200 K, and the photospheric velocity is 9200 km s^{-1}. This layer of the ejecta requires no carbon, and is dominated by oxygen (50%). In this shell the S abundance drops to 5%, whereas the Si abundance increases to 35%. This is unusual for a SN Ia as one would expect S to propagate to slightly lower velocities than Si as a consequence of the nucleosynthesis reaction chain described by Nomoto et al. (1984). However, the S II feature at 5640 Å is fit almost perfectly by the model at this epoch, and increasing the S abundance would worsen the fit. It should be noted that in the abundance distributions of SNe 2004eo and 2011fe the S abundance does not

[1] 0.12 mag of this is from foreground galactic extinction (Schlafly & Finkbeiner 2011)

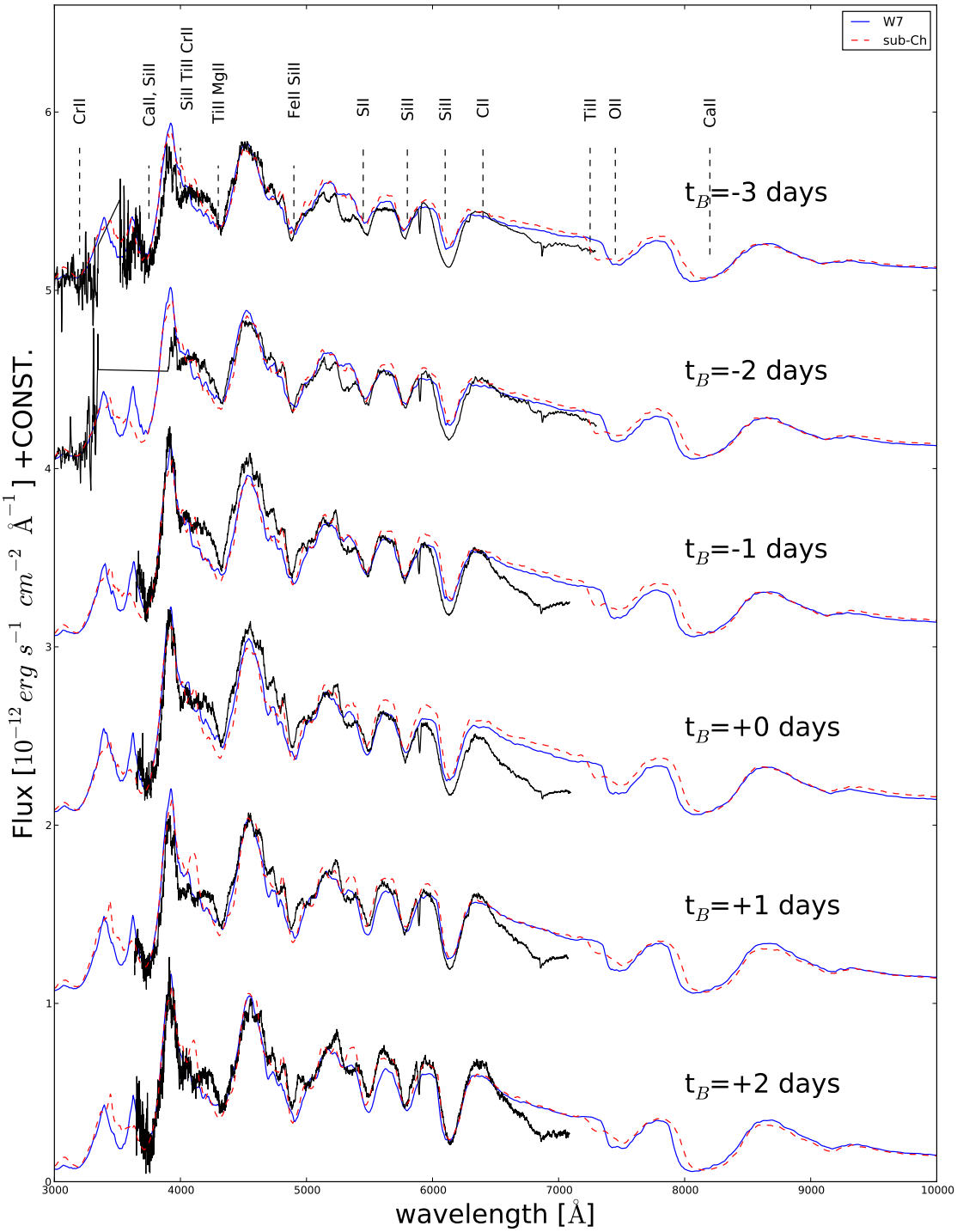

Figure 4. The photospheric phase models of SN 1986G, where the spectra have been shifted in flux by a constant for clarity. Models for both the W7 (blue solid) and Sub-Ch (red dashed) density profiles are shown. The spectra have been corrected for extinction.

Table 4. Input parameters and calculated converged black body temperatures for models from the W7 and Sub-Ch density profiles.

Epoch t_{rise}	velocity v_{ph}	Bol Lum L	Temperature T_{BB}	velocity v_{ph}	Bol Lum L	Temperature T_{BB}
days	$km\,s^{-1}$ W7	$logL_{\odot}$ W7	K W7	$km\,s^{-1}$ Sub-Ch	$log(L_{\odot})$ Sub-Ch	K Sub-Ch
15	10000	8.960	8900	10000	8.96	9100
16	9400	8.990	9100	9200	9.00	9500
17	8800	9.040	9500	8900	9.040	9600
18	8100	9.060	10000	8500	9.070	9700
19	7800	9.050	9700	7200	9.050	10300
20	7600	9.050	9500	7000	9.050	10100

propagate as deep as that of Si (Mazzali et al. 2008, 2015). Using the Sub-Ch density profile the abundances of Ti+Cr (8%) and Fe (1.3%) are higher than those needed for the W7 model. The Ti +Cr abundance is required to be this high to fit the blue ward edge of the 4200Å feature. Without this high abundance there is no absorption at 4100Å .

4.6 -1 days

The third spectrum in Figure 4 was taken at -1 day relative to *B* band maximum. This spectrum was modelled as 17 days after explosion. The synthetic spectrum produced using the W7 density profile is a very good fit to the observed one. The feature at ∼4900Å has resolved into separate Fe II lines, and the W7 density profile fits all of these lines at the correct velocities. The photospheric velocity at this epoch is 8900 kms^{-1}, with a bolometric luminosity of 42.63 $\mathrm{erg\,s}^{-1}$ and a T_{eff} of 9200 K. This shell is still dominated by oxygen, however at this epoch the abundance of oxygen is starting to decrease. The oxygen fraction is 50% by mass. The Si abundance has increased to 35%, and that of Ti+Cr to 1.5%.

The Sub-Ch model has v_{ph} = 8900 kms^{-1} and a bolometric luminosity of $\log_{10}L$=42.60 $\mathrm{erg\,s}^{-1}$. At this epoch oxygen still dominates at 44%, but IMEs also significantly contribute to the spectrum (Si 37%, S 5%, Ca 2%). Relative to the previous epoch the Ti+Cr abundance has decreased to 6.5%, but the Fe abundance has increased to 5%. The effective temperature at this epoch is 9400 K.

4.7 +0 days

IMEs begin to dominate the ejecta at this epoch, which is at *B* band and bolometric maximum. For the W7 model, the Si and S abundances are 65% and 13%, respectively. This spectrum was computed with a photospheric velocity of 8100 kms^{-1} and a bolometric luminosity of $\log_{10}L$=42.65 $\mathrm{erg\,s}^{-1}$. The effective temperature at this epoch is 9700 K. The combined Ti+Cr abundance has increased to 1.8%.

The Sub-Ch model for this spectrum has a $\log_{10}L$=42.66 $\mathrm{erg\,s}^{-1}$, a v_{ph} = 8500 kms^{-1} and an effective temperature of 9600 K, the photospheric velocity has hardly changed compared to the previous epoch. IMEs also begin to dominate the Sub-Ch model (Si 40%, S 5%, Ca 8%).

4.8 +1 days

This spectrum was observed at +1 day relative to *B* band maximum. The photospheric velocity (7800 kms^{-1}) has only slightly decreased (by 300 kms^{-1}) compared to the previous epoch. The model at the epoch has a luminosity of $\log_{10}L$=42.64 $\mathrm{erg\,s}^{-1}$. Because of the small change in photospheric velocity from the previous epoch there is practically no spectral evolution. Therefore the abundances have not changed significantly. The effective temperature of this shell is 9600 K.

The Sub-Ch model at this epoch contains no S near the photosphere, although there is still 34% of oxygen left in the ejecta. This may indicate that the Sub-Ch density is not a good solution and cannot explain the mechanism and progenitor of SN 1986G. There is an increase in Fe abundance at this epoch (7%), and the Ti+Cr abundance is 4%. The effective temperature of the Sub-Ch model is 10200 K. The model at the epoch has a luminosity of $\log_{10}L$=42.64 $\mathrm{erg\,s}^{-1}$, and a photospheric velocity of 7200 kms^{-1}.

4.9 +2days

The last W7 photospheric model for the spectrum at +2 days (20 days from explosion). It is shown in Figure 4. It has a v_{ph}=7600 $\mathrm{km\,s}^{-1}$, T_{eff}=9300 K and $\log_{10}L$=42.62 $\mathrm{erg\,s}^{-1}$. This shell has 75% Si and 10% S. The Ca abundance is set at 0.3%.

The final Sub-Ch model still has a large mass of oxygen (30%), but this epoch is dominated by Si (56%). The Ti and Cr abundances have stayed constant, but the Fe abundance has increased to 8%. The effective temperature at this epoch is 10100 K. There are some doubly ionized species in the spectrum at this time, Fe III and Cr III in the features at ∼5000Å and ∼3700Å respectively. These doubly ionized species correspond to the effective temperature increase, compared to the +1 days model. The W7 model has fewer doubly ionized species.

At every epoch in the Sub-Ch model there is a deep Ti II absorption at ∼7300Å.This feature is not seen in the W7 models, nor in the observed spectrum, and it is produced because the Sub-Ch model has more mass at high velocities. It is another indication the Sub-Ch density profile is a poor solution compared to the W7 model. However, apart form this feature, it could be argued that the Sub-Ch density profile produces better fits. The full input parameters for the photospheric models can be found in Table 4. The

photospheric velocity of SN 1986G is lower than what would be expected for a normal SNe Ia. The photospheric phase models probe layers above 7000 km s^{-1} in velocity. The bolometric luminosity of the models peak at +0 days compared to *B* band maximum, which is expected from a SN with a steep light curve.

5 NEBULAR PHASE MODELS

A single nebular spectrum of SN 1986G is available, which was published by Cristiani et al. (1992) and was obtained ~ 256 days after maximum. The spectrum shows the usual nebular SN Ia features, strong Fe II and Fe III lines in the blue and a mix of Ca II and Fe II lines in the red. It is significantly affected by reddening, to the point of showing self-absorption in the NaID line as well as a narrow Hα absorption in the middle of a weak Fe II emission complex. As a result of the large amount of reddening, lines in the blue appear to be suppressed.

We have completed the abundance tomography experiment modelling the nebular spectrum using two different density distributions: the original W7 model and the Sub-Ch model discussed above.

We used the nebular spectrum code which has been used in the past to model both SNe Ia (e.g. Mazzali et al. 2015) and SNe Ib/c (e.g. Mazzali et al. 2007a, where a more detailed description of the code can be found). The code computes the diffusion and deposition of gamma-rays and positrons produced by the radioactive decay of ^{56}Ni and ^{56}Co in the SN ejecta using gray opacities in a montecarlo scheme. The ensuing collisional heating of the SN ejecta is then balanced by cooling via line emission, following Axelrod (1980). The balance between radiation and gas properties is computed in non-local thermodynamic equilibrium (NLTE). The abundances in the ejecta were adjusted to optimise the fit, except at the velocities where abundances were determined from early-time spectral modelling. These are regions with velocities above 7000 kms^{-1}, which are not sampled by the nebular emission lines. A simple one-zone fit to the spectrum yields a model line velocity of 5600 kms^{-1}, which is also in line with the fast evolution of the light curve of SN 1986G (Mazzali et al. 1998, 2007a).

The two best-fit models are shown in Figure 5. Although the models are overall quite similar in the kind of emission lines that are predicted, there are significant differences which can help us discriminate among them. The individual models are discussed in turn.

The W7 model (dashed/blue line) produces a good match in particular to the blue part of the spectrum. A ^{56}Ni mass of 0.13 M$_\odot$ is required. Because the inner region in W7 is quite dense, material other than ^{56}Ni must be used to fill it. Stable Fe-group elements are produced in the centre of Chandrasekhar-mass explosions, and we find that a total mass of about 0.11M$_\odot$ is required. This is dominated by stable Fe. Stable Fe-group material is important as is acts only as a coolant, so its presence contributes to balancing the heating from radioactive decay and to keeping the ionization ratio (in particular Fe III/Fe II) close to the observed value. The mass included within a velocity of 5600 kms^{-1} in W7 is ~ 0.4$M_\odot$, and NSE material does not reach this value. The remaining mass is attributed to intermediate-mass elements, in particular Si, which leads to a strong predicted emission in the NIR, near 1.6μ m. The line near 5900 Å is predominantly NaID. The strong emission near 7300 Å is well reproduced as a combination of Fe II and Ca II with a minor contribution from Ni II . The narrowness of the emission lines leads to the observed split between the two features. In fact, a hint of a split can be seen even in the emission feature near 5200 Å, and this is due just to lines separating out, as in, e.g., SN 2003hv (Mazzali et al. 2011), not to double peaks caused by the morphology of the explosion. Other Fe II lines are not well reproduced, though. In particular, the feature near 6600 Å is too weak in the model, while the broad blend near 9000 Å is too strong. These shortcomings are seen in most of our SN Ia models, but to a much lesser degree (e.g. Mazzali et al. 2015). They may partially depend on uncertain collisional rates, and they indicate that the ^{56}Ni mass may be slightly overestimated. On the other hand, the extreme deviation of the redder lines in SN 1986G may also indicate problems with the density structure (see e.g. Mazzali et al. 2011), or issues with the red part of the observed spectrum. Note that in a well-observed SN Ia like SN 2011fe the ratio of the Ca-Fe emission near 7300 Å and that of the Fe complex near 9500 Å is ~ 1. In the spectrum of SN 1986G, after correcting for reddening, the ratio is ~ 2, but our model has a ratio of ~ 1. Unfortunately no other nebular spectrum is available of either SN 1986G or of SNe that closely resemble it, so we cannot verify this.

The Sub-Ch model (green line), compared to the W7 one, has several problems. Primarily, the ionization of Fe is too high. This is shown by the excessive strength of the emission near 4700 Å when the model matches that at 5200 Å. Note that the model displayed is reddened, which depresses the bluer feature significantly. This behaviour was seen in a peculiar SN like 2003hv (Mazzali et al. 2011), and was interpreted there to indicate low densities at low velocities, which is exactly what a Sub-Ch model predicts, and a consequent lack of stable NSE material, leading to insufficient cooling and hence recombination. The Fe II lines in the red are actually depressed relative to the line at 5200 Å. The model contains only ~ 1 M$_\odot$. Most of the missing mass is stable NSE material, the mass of which has gone down to 0.1 M$_\odot$, mostly stable Fe at intermediate velocities. Intermediate-mass elements just above the ^{56}Ni zone again lead to strong Si emission in the NIR. The incorrect ratio of the optical Fe lines is a strong argument against this model, which we do not favour.

6 ABUNDANCE TOMOGRAPHY

Figures 6 and 7 show the abundance distributions of SN 1986G as a function of velocity and enclosed mass. At velocities below 7000 kms^{-1} the nebular modelling determines the distribution, and at velocities above 7000 kms^{-1} the photospheric models determine the distribution. Above ~12000 kms^{-1} certain aspects of the distribution can be inferred, but this is where the results are most uncertain because early data are not available. However, incorrect abundances in the outer layers can make it impossible to produce a good synthetic spectrum in the inner layers, so we can assume that the description of the outer layers is not completely unreasonable.

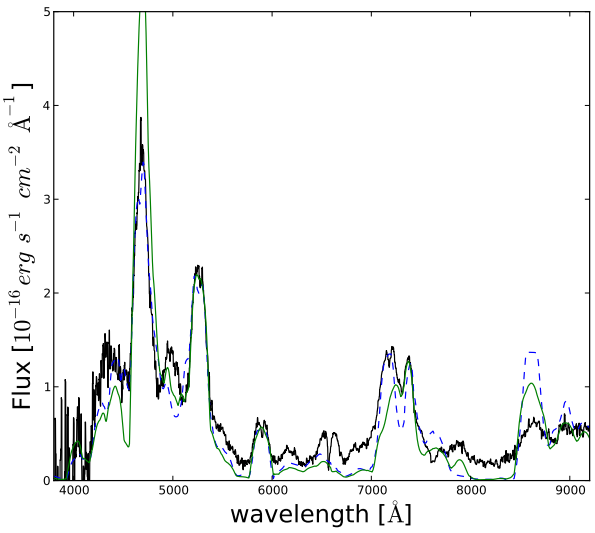

Figure 5. The nebular phase models of SN 1986G. The blue spectrum was obtained using a W7 density profile and the green spectrum using the Sub-Ch profile. The black line is the observed spectrum. The spectra have been corrected for extinction.

Figure 6 is the abundance distribution produced using the W7 density profile. An upper limit to the abundance of carbon is set to a mass of 0.02 $M_\odot$. All of this progenitor carbon is at high velocities, >10000 kms^{-1}. The outer layers of the ejecta are dominated by oxygen, which is seen throughout the whole of the photospheric phase, but the part of the observed spectra where we would expect to see oxygen, ~7500 Å, was not observed. It is reasonable to infer a high oxygen abundance in SN 1986G, because of its similarities with 91bg-like SNe, which show a strong oxygen feature.Furthermore, the fact that we detect carbon in the spectra is a good indication that oxygen will be present between layers where the carbon and IME dominate. The final masses from the W7 abundance distribution can be found in Table 5. Masses have been quoted to the second decimal place, but does not mean accuracy to this degree. It is required as there are elements which do not have a mass greater than 0.1 $M_\odot$. IMEs dominate the abundance distribution of the SN at intermediate velocities. The S distribution follows the Si distribution at velocities down to ~7000 kms^{-1}, with a lower ratio than traditionally would be expected. The typical ratio of Si to S is 3 to 1. The S abundance drops to 0 at v ~6000 kms^{-1}. The enclosed mass range in which Si dominates is from 0.75 $M_\odot$ to 0.19 $M_\odot$. This is very different from SN 1991T, which sits at the opposite end of the 'Phillips Relation', where Si dominates only in the enclosed mass range of ~1.05 $M_\odot$ to 1.07 $M_\odot$ (Sasdelli et al. 2014). The large amount of Si in SN 1986G corresponds to a small amount of ^{56}Ni being produced in the explosion (Mazzali et al. 2007a). This agrees with SN 1986G having a low luminosity and partial burning. There is no evidence for mixing of ^{56}Ni to high velocities for SN 1986G. A ^{56}Ni mass of 0.13 $M_\odot$ is obtained from the abundance distribution. Most ^{56}Ni is located in the denser inner layers. At velocities between 1000 km s^{-1} and ~ 3500 km s^{-1} Fe and ^{56}Ni dominate the ejecta. The innermost layers of the SN 1986G W7 density profile model are dominated by stable Ni, and ^{56}Ni is further out in the ejecta, between an enclosed mass of ~0.1 and ~0.55 $M_\odot$. This is consistent with the burning that a fast deflagration such as that of a W7-like model predicts. The Ti+Cr abundances peak in the velocity range 8000-9000 kms^{-1}. Their combined integrated mass is of the order of 0.01 $M_\odot$.

Table 5. Integrated abundances from the full abundance tomography modelling of SN 1986G. The errors on the masses are ±25%, except for ^{56}Ni which has an error of ±10%.

Element	W7 $M_\odot$	Sub-Ch $M_\odot$
C	0.02	0.04
O	0.49	0.51
Mg	<0.01	<0.01
Si	0.50	0.26
S	0.05	0.04
Ca	0.02	0.01
Ti+Cr	0.01	0.02
Fe	0.11	0.09
^{56}Ni	0.13	0.11
Ni	0.04	0.01
M_{tot}	1.38	1.11

The abundance distribution produced using the Sub-Ch density profile is dramatically different from that of the W7 density profile, as shown in Figure 7. The total C mass is 0.04 $M_\odot$. There is evidence for carbon down to an enclosed mass of ~0.7 $M_\odot$. The outer layers consist almost entirely of oxygen. The oxygen zone is large compared to a normal SN Ia. Oxygen dominates down to 6000 km s^{-1}, and is present down to velocities as low as 4000 kms^{-1} with abundances of the order of 20%. Between 6000 km s^{-1} and 4000 km s^{-1} IMEs dominate, and NSE material dominates the inner layers of the ejecta. The total amount of ^{56}Ni in the ejecta of SN 1986G, assuming a Sub-Ch density profile, is 0.11 $M_\odot$. The abundance distributions produced using the Sub-Ch model implies that this explosion scenario is not a valid one for SN 1986G. Oxygen probes to deeper layers of the ejecta than sulphur, which is in direct conflict with nucleosynthesis calculations and expected results. The zone where IMEs dominate has an unusually small velocity range of 500 kms^{-1}. Overall, the abundance yields and distribution from the Sub-Ch model do not agree with nucleosynthesis and explosion models.

7 A CONSISTENT, REDUCED-ENERGY MODEL

7.1 Energy estimates

With the integrated masses obtained form the abundance tomography modelling, the kinetic energy of the explosion can be derived, using the formula

$$E_k = [1.56(^{56}Ni) + 1.74(stableNSE) + 1.24M(IME) - E_{BE}]10^{51}\ erg \quad (1)$$

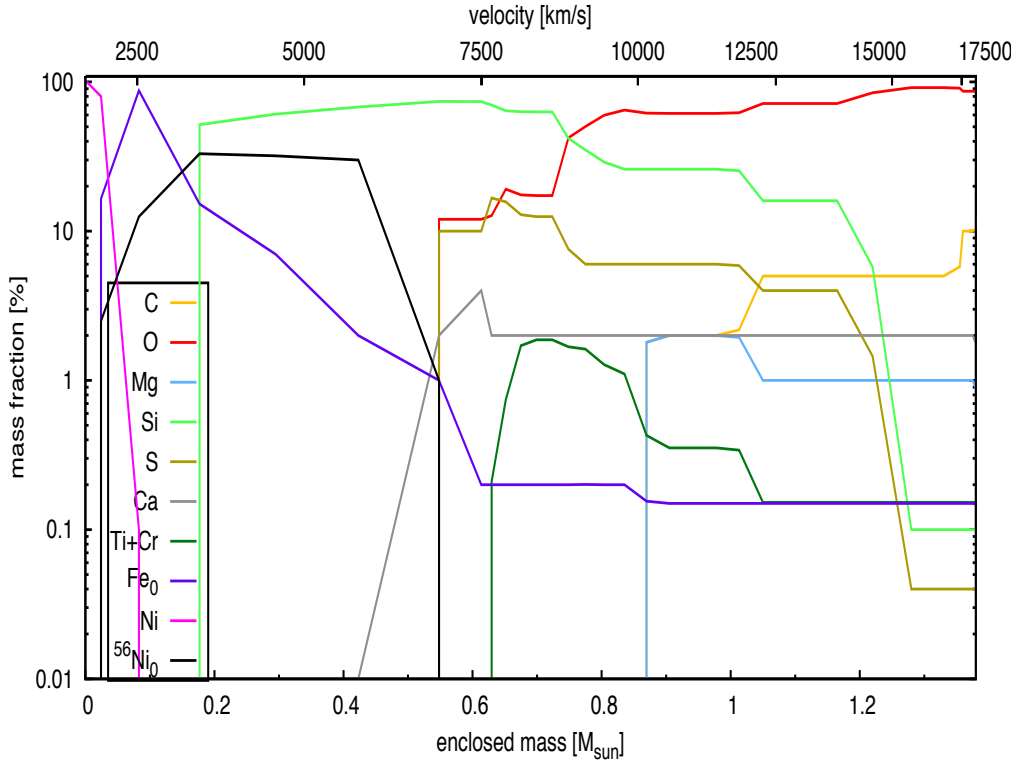

Figure 6. The final abundance distribution of SN 1986G obtained with the W7 density profile.

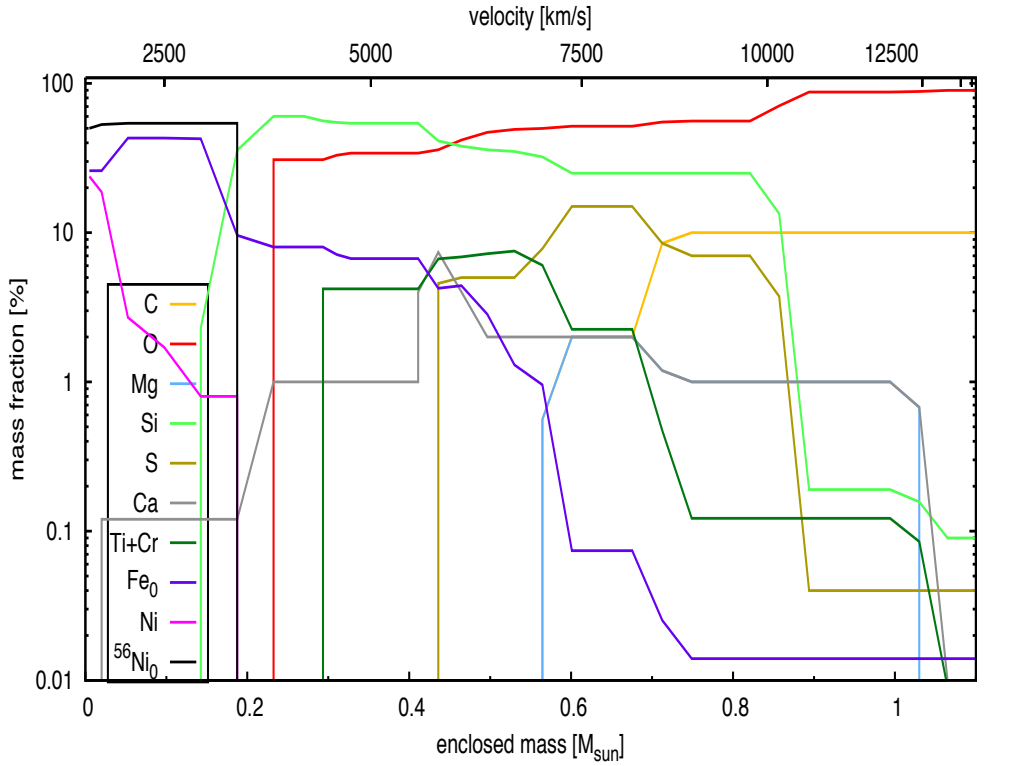

Figure 7. The final abundance distribution of SN 1986G obtained with the Sub-Ch density profile.

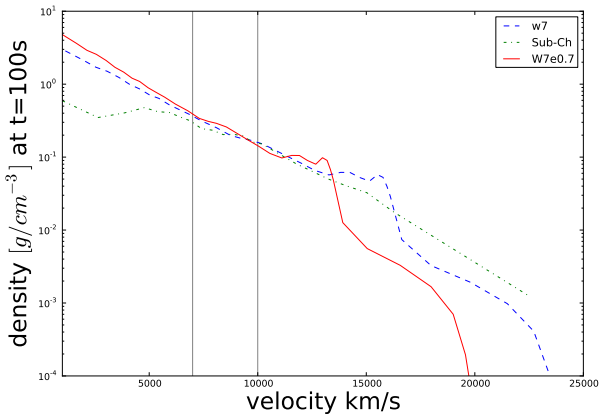

Figure 8. The W7, Sub-Ch and W7e0.7 density profiles as a function of velocity at t=100 s after explosion. The vertical grey lines show the range in values v_{ph} can take, for the -3 d to +2 d models.

(Woosley et al. 2007). Where E_{BE} is the binding energy of the progenitor white dwarf, ^{56}Ni is the ^{56}Ni mass in the ejecta, stableNSE is the stableNSE mass is the ejecta and M(IME) is the total IME mass in the ejecta. We find that the $E_{\rm kin}$ of the explosion is 0.8×10^{51} erg, using the masses derived by the W7 density profile model [2]. The $E_{\rm kin}$ calculated from the abundances obtained using the W7 density profile is smaller than the value for the standard W7 explosion, which has $E_{\rm kin}$ = 1.3×10^{51} erg. Therefore, there is a discrepancy between the input density profile and the $E_{\rm kin}$ derived from the nucleosynthesis. This discrepancy is an issue if one wants to solve the progenitor scenario and explosion mechanism of SN 1986G. For the Sub-Ch density model $E_{BE} = 0.21 \times 10^{51}$ erg (Yoon & Langer 2005), which equates to a $E_{\rm kin}$ of 0.55×10^{51} erg (the $E_{\rm kin}$ of the Sub-Ch explosion model that we used is 1.2×10^{51} erg), so again the model has a larger $E_{\rm kin}$ than what we infer from the nucleosynthesis.

We therefore attempted to develop a density profile that both fits the spectra and is consistent with the nucleosynthesis. Given what we discussed above, this has to be a low energy density profile. In this section we build and test such a profile. We did this by scaling the W7 density profile to a lower $E_{\rm kin}$ using equations 2 and 3.

$$\rho' = \rho_{W7}\Big(\frac{E'}{E_{W7}}\Big)^{-\frac{3}{2}} \cdot \Big(\frac{M'}{M_{W7}}\Big)^{\frac{5}{2}} \quad (2)$$

$$v' = v_{W7}\Big(\frac{E'}{E_{W7}}\Big)^{\frac{1}{2}} \cdot \Big(\frac{M'}{M_{W7}}\Big)^{-\frac{1}{2}} \quad (3)$$

In these equations ρ' is the new density, ρ_{W7} is the W7 density, E' is the energy of the new density profile, E_{W7} is the energy of the W7 density profile, M' is the mass of the new density profile and M_{W7} is the mass of the W7 density profile, v_{W7} is the velocity of W7 the density profile, and v' is the velocity of the new profile.

[2] For a Chandrasekhar mass WD $E_{BE} = 0.46 \times 10^{51}$ erg.

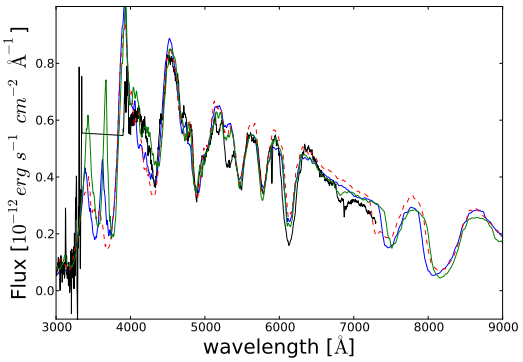

Figure 9. One-zone models at -3 days relative to B band maximum. The synthetic spectra were produced using the W7 (blue), W7e0.7 (green) and Sub-Ch (red dashed) density profiles. The spectra have been corrected for extinction.

The density profile was scaled keeping the mass at the Chandrasekhar mass and scaling the energy to 70% of that of the W7 density profile to match the $E_{\rm kin}$ inferred from the nucleosynthesis, and for convenience it is called W7e0.7. This rescalilng has been shown to work well for SN 2005bl. However, this SN was only modelled in the photospheric phase (Hachinger et al. 2009), as late-time spectra were not available. Therefore, placing the mass in the inner layers may not have been the perfect solution (see Mazzali et al. 2011). In contrast, SN 1986G has good nebular data, so it is possible to tell if this increase in central density can be a realistic solution.

Figure 8 shows the W7, Sub-Ch and W7e0.7 density profiles at t=100 s after the explosion. Compared to W7, the Sub-Ch density profile has more mass at higher velocities and a lower central density, whereas the W7e0.7 model has a higher central density and less material at high velocities, and hence a smaller $E_{\rm kin}$. To decrease the energy in the W7 model, the mass which was removed from the high velocities was redistributed to the inner part of the ejecta.

7.2 Photospheric-epoch models

Figure 9 shows the synthetic spectra produced with all three density profiles at -3 days relative to B band maximum. The green line is the W7e0.7 model. This model fits the data (black line) very well, the Si II line ratio is correct, and the sulphur and Fe features are fit almost perfectly. The fact that the W7e0.7 density profile produces a good fit is reason for the full abundance tomography analysis to be carried out using the W7e0.7 density profile, with the aim of getting a consistent model.

The full photospheric models obtained with the new, W7e0.7, density structure are presented in Figure 10. The synthetic spectra are better than the Sub-Ch and W7 equivalent. The models were remade using the same input parameters as those for the W7 model in Table 4. The only elements which changed in abundance, in velocity space, were Ti+Cr, with their mass fraction increasing to ~ 3% at 8000 km s^{-1}. In the W7e0.7 spectra, the ratio of the strongest Si II features (6355 and 5970 Å) has improved and the Ti 4450 Å feature fits significantly better. These improvements could

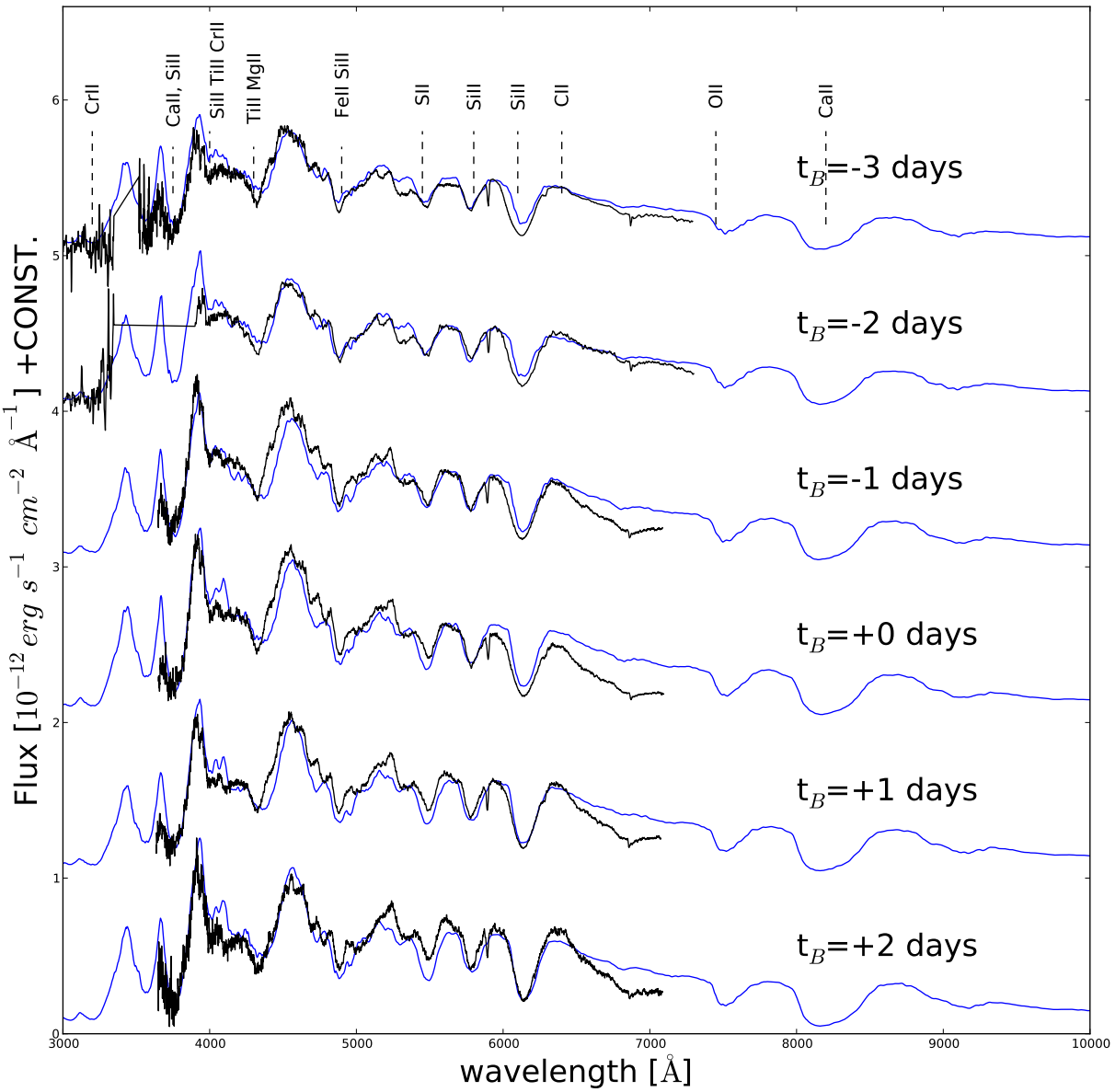

Figure 10. The photospheric phase models of SN 1986G, calculated using the W7e0.7 density profile. The blue line are the models and the black line the observed spectra. The spectra have been corrected for extinction.

be caused by the bump in the density profile moving inwards in velocity space. This causes there to be an increase in density closer to the photosphere. This bump is still in the oxygen zone, but there is also an increase in the Si abundance. The improvements are also due to a lack of material at high velocities. It is apparent that a steeper density than the standard W7 model is required above 12500 kms^{-1}.

7.3 Carbon

From Figure 4 it is apparent at -3 and -2 days that there is some C II in the spectra, at ~ 6350Å. As there are no observed spectra before -3 days it is not possible to put an exact constraint on the amount of unburnt carbon in the ejecta, therefore in the next part of the analysis we attempt to constrain an upper limit on the C abundance. The

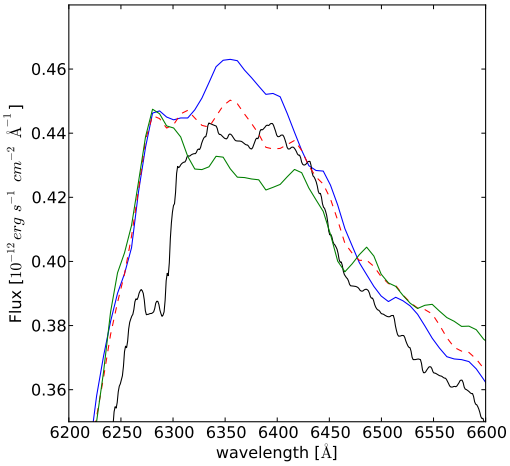

Figure 11. Synthetic spectrum at -3 days produced using the W7e0.7 density profile to constrain an upper limit on carbon. The blue line is the model with 0% of C, the red dashed line with the 2% C and the green line with 10% C at the photosphere. The black line is the observed spectra.

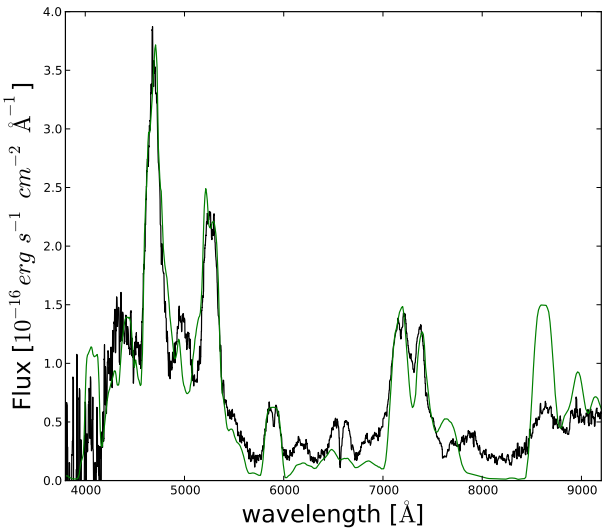

Figure 12. The nebular phase models of SN 1986G. The green line is the model calculated using the W7e0.7 density profile. The spectra have been corrected for extinction.

synthetic spectra produced using the W7e0.7 density profile has 3 synthetic shells based above the -3 days, 10000 kms^{-1}, outer shell. The purpose of having these synthetic layers is to produce a stratified abundance distribution. If the distribution is not stratified the model spectra will produce a poor fit. Figure 11 shows the -3 day spectrum over a wavelength range of 6200-6600 Å, where unburnt carbon would be seen in the ejecta. In order to produce the best fit of this C II feature the W7e0.7 model requires a carbon abundance of 13% at 23000 kms^{-1}, 10% at 17550 kms^{-1}, 5% at 12000 kms^{-1} and 2% at 10000 kms^{-1}. Increasing the 12000 kms^{-1} layer to an abundance of 12% produces the green line in Figure 11, and having zero carbon in the ejecta produces the blue line in Figure 11, both of which yield a worse fit. When determining the best fit it is important to only examine the spectra between 6300-6450Å as this is where the C II λ6578 and λ6582 lines will be seen, blue-ward of this is Si II absorption and red-ward is continuum. The integrated carbon mass abundance from the best fit using the W7e0.7 density profile is 0.02 M$_\odot$.

7.4 Nebular-epoch model

A nebular phase model was produced using the W7e0.7 density. It is shown as a green line in Fig. 12. This density profile has more mass at low velocity (~ 0.50 M$_\odot$ within 5600 kms^{-1} as opposed to ~ 0.40 for W7). The ^{56}Ni mass is now ~ 0.14 M$_\odot$, but the higher density at low velocities results in a larger mass of stable NSE material, ~ 0.21 $M_\odot$, most of which is stable Fe. This is in line with Mazzali et al. (2007a). The additional cooling provided by the stable NSE material leads to the correct reproduction of the Fe II/Fe III line ratio in the blue, but it does not solve the problem of the excessive Fe II emission in the red, where the synthetic spectrum predicts excessively strong lines. As we argued above, there may be a problem with our model, but also with the redder part of the observed spectrum itself. Nebular-epoch observations of SN 1986G-like SNe are encouraged in order to assess the reality of the red flux.

7.5 Abundance stratification

The abundance stratification of the W7e0.7 model can be seen in Figure 13. The oxygen layer dominates the ejecta down to velocities of ~ 9000 km s^{-1}. IMEs dominate the bulk of the ejecta in at velocities between ~ 9000 km s^{-1} and ~ 3500 km s^{-1}. Below ~ 3500 km s^{-1} NSE material dominates, with the ejecta consisting entirely of stable Ni in the innermost 1000 km s^{-1}. ^{56}Ni is more evenly distributed than in the W7 model. The ^{56}Ni abundance peaks at 40% in the velocity range 4000 – 6000 $km\ s^{-1}$. It is also seen in the ejecta down to a velocity of 1000 kms^{-1}. In the models produced using the W7 and Sub-Ch density profiles oxygen probes to deeper layers of the ejecta than sulphur, which is in direct conflict with SNe Ia nucleosynthesis calculations and explosion models (Iwamoto et al. 1999). However, in the W7e0.7 model sulphur is required down to a velocity of ~4000 kms^{-1}, and oxygen is only seen down to velocities of ~ 6000 kms^{-1}, so the problem no longer exists.

The abundance distribution from the W7e0.7 model produces physically sensible results, as well as good fits between the observed and synthetic spectra. The integrated masses obtained using this density profile can be found in Table 6. The Ni mass is 0.14 M$_\odot$, with IMEs making up 0.69 M$_\odot$ and 0.34 M$_\odot$ of unburnt material. Using equation 1 the kinetic energy of the ejecta can be calculated. The $E_{\rm kin}$ calculated using this method is 0.97×10^{51} erg, which is consistent with the energy of the W7e0.7 density profile (0.9×10^{51} erg).

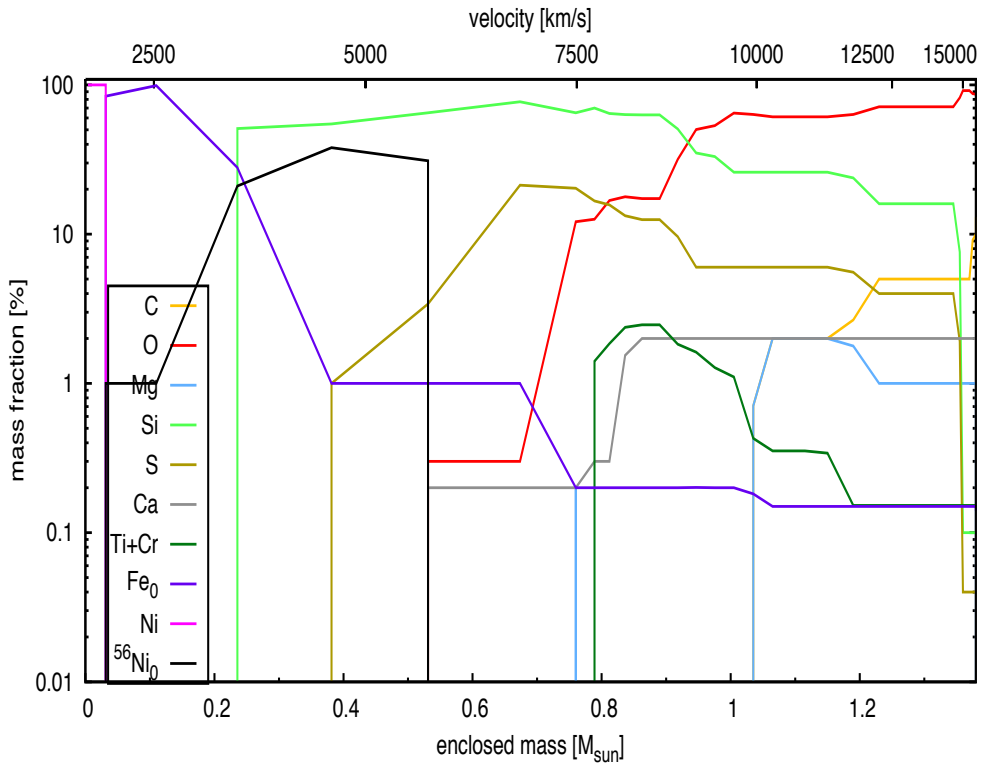

Figure 13. The abundance distribution of the ejecta of SN 1986G obtained using the W7e0.7 density profile.

Table 6. Integrated abundances the the models which used the W7e0.7. The errors on the masses are ±25%, except for ^{56}Ni which has an error of ±10%.

Element	W7 E70% $M_\odot$
C	0.01
O	0.33
Mg	<0.01
Si	0.58
S	0.09
Ca	0.01
Ti+Cr	0.01
Fe	0.18
^{56}Ni	0.14
Ni	0.02
M_{tot}	1.38

8 BOLOMETRIC LIGHT CURVES

8.1 Observed light curve

We have constructed a bolometric light curve of SN 1986G in the range 3000-24000 Å, covered by our optical and NIR photometry, and used the well-monitored SN Ia 2004eo as a proxy.

As a first approach, we dereddened the optical (*UVB*) and NIR (*JHK*) light curves of SN 1986G using $E(B-V)_{tot}$ = 0.65 and the extinction curve of Cardelli et al. (1989). We then splined these points with a time resolution of 1 day and constructed daily spectral energy distributions in the above wavelength interval using the flux zeropoints of Fukugita et al. (1995). For each epoch, we integrated the flux between the U and K bands after interpolating the flux between the central wavelengths of the filters, and added at the blue and red boundaries of the interval the fluxes obtained by extrapolating the spectrum with a flat power-law to 3000 and 24000 Å, respectively. We then resampled the final bolometric LC to the epochs of the actual V-band observations.

The lack of significant coverage in *R* and *I* bands (only a couple of points are available in each of these bands) represents a serious drawback, because the interpolation between *V* and *J* bands overestimates the *R* and *I* flux. Therefore, the final bolometric LC must be considered as an upper limit to the "real" one (which we will call '$UL_{bol}86G$'). On the other hand, if we only integrate separately the flux in *UBV* and in *JHK* filters over the 3000-6000 Å and 10000-24000 Å ranges, respectively, and sum these two broad-band fluxes, we neglect completely the flux contribution in *R* and *I* bands, so that the resulting bolometric LC must be considered as a lower limit of the true one ('$LL_{bol}86G$'). Clearly, the real bolometric LC must be somewhere between $UL_{bol}86G$ and $LL_{bol}86G$.

To evaluate the necessary bolometric corrections in the most rigorous way possible and thus to obtain a reliable estimate of the bol LC of SN 1986G, we have resorted to the SN Ia 2004eo, which had good coverage in all bands between *U* and *K* (Pastorello et al. 2007; Mazzali et al. 2008), as an analogue of SN 1986G. Since *U* and *JHK* bands coverage

for SN 2004eo is only available after maximum, we reconstructed the flux in these bands before maximum assuming that the $U-B$, $J-I$, $H-I$ and $K-I$ colours before maximum are constant and equal to the values they have at maximum (we have verified a posteriori that this has a negligible effect with respect to simply ignoring the $UJHK$ band before maximum in the computation of the bolometric flux). The $UBVRIJHK$ light curves of SN 2004eo, dereddened with $E(B-V) = 0.109$, were splined with a time resolution of 1 day, and spectral energy distributions were constructed and integrated over the range 3000-24000 Å, as for SN 1986G. This is our reference bolometric light curve, which we will call our 'template' bolometric LC.

We have then constructed two more bolometric light curves for SN2004eo in the same wavelength intervals as ULbol86G and LLbol86G above, and ignoring the R and I bands: first we interpolated the spectral flux between V and J - we will call this ULbol04eo - and then we summed the spectral flux in the UBV filters (3000-6000Å) and in the JHK filters (10000-24000Å). We will call this latter bolometric LC LLbol04eo. Bolometric corrections for SN 2004eo with respect to the 'template' were computed by simply differencing the template and its upper ($UL_{bol}04eo$) and lower ($LL_{bol}04eo$) limits. Then, these differences were applied, with their signs, to the limits obtained for SN 1986G, $UL_{bol}86G$ and $LL_{bol}86G$, so that 2 'corrected' bolometric LCs for SN 1986G were obtained. What we consider the 'real' bolometric LC of SN 1986G was obtained by averaging these 2 'corrected' bolometric light curves.

8.2 Synthetic light curve

In the spirit of abundance tomography, we now combine the density distributions that we used and the abundances derived through synthetic spectra fitting and compute a bolometric light curve, which we compare to the one constructed based on the observed SN photometry. We use a montecarlo code (Cappellaro et al. 1997) which computes the emission of gamma-rays and positrons following the radioactive decay of ^{56}Ni and ^{56}Co and their deposition in the ejecta. The ^{56}Ni distribution is derived from the spectral fitting. Gamma ray deposition is computed with a grey opacity of $0.027\,\mathrm{cm^2\,g^{-1}}$, and for positrons a grey opacity $7\,\mathrm{cm^2\,g^{-1}}$ is used.

After deposition of the gamma-ray and positron energy, the resulting energy is assumed to be thermalised and energy packets representing photons are then followed as they propagate through the SN ejecta. The opacity they encounter is assumed to be dominated by line opacity and is parametrised according to the relative abundances at different depths according to the number of active lines as in Mazzali (2000):
$\kappa = 0.25Ab(Fe-gp) + 0.025 \times (1 - Ab(Fe-gp))$

The results for the different models are shown in Figure 14 along with the observationally derived bolometric light curve. At peak, the Sub-Ch model (red/dot-dashed line) reaches maximum within 12-13 days, which appears to be a short time compared to the observed light curve. The early declining part of the light curve also happens too early in this model, but then at epochs between 60 and 300 days this model follows the data reasonably well, although it underestimates the luminosity because of the low gamma ray depositions. At late times, the light curve matches the data at 275 days, and is again too low later on, but at these epochs the observed light curve declines unusually slowly.

Both Chandrasekhar-mass models, on the other hand, reach maximum after about 17-18 days, which is in line with the observed light curve and the results from spectroscopic modelling. These models also follow the early light curve decline quite well, but then are more luminous than the observed light curve by almost a factor of 2 after about day 60. At late times they finally rejoin the observed light curve, but they have a different slope. Looking in more detail, the low-energy model (purple/continuous line) is somewhat more luminous than the W7 model (green/dashed line) after day 60, because of the enhanced gamma-ray deposition resulting from the higher densities in the more slowly expanding ejecta. This difference is however quite small, such that neither model can be favoured over the other. The indications for a low energy from spectral fitting are therefore not disproved by the light curve model.

The real issue is the behaviour of the light curve, first after 60 days and then at late times. The steep decline after day 60 is not in line with the behaviour of other SNe Ia, (Mazzali et al. 2007a, e.g. SN 2004eo), which suggests that the IR contribution is not known. The range of possible corrections does in fact allow a much higher luminosity. At the latest times the decline is quite slow, possibly indicating incorrect background subtraction. The one point when spectra are available still suffers from the lack of IR information. Again, observations of a modern 1986G-like SN Ia would be needed to improve both the data coverage and the modelling results.

Yet, our results indicate that a low-energy Chandrasekhar-mass model is favoured over an under-massive model, which may come somewhat as a surprise given that SN 1986G showed quite a rapidly evolving light curve. We argue that the rapid light curve evolution is the result of the low opacity, as a consequence of the low NSE elements abundance ($\sim 0.35 M_{\odot}$).

9 CONCLUSIONS

A full theoretical spectral analysis of SN 1986G has been performed, using the 'abundance tomography' approach. SN 1986G bridges the gap between a normal and subluminous SN Ia. It is found that the ejecta of SN 1986G have a low temperature and are dominated by singly ionised IMEs. Three density profiles were tested, a standard Chandrasekhar mass delayed detonation (W7) density profile, a low energy Chandrasekhar mass delayed detonation (W7e0.7) density profile and a Sub-Chandrasekhar mass detonation density profile (Sub-Ch).

The Sub-Ch models produce good photospheric phase synthetic spectra, but this density profile can be ruled out owing to the unrealistic abundance distribution and poor synthetic nebular spectra. Furthermore, the W7 density profile is found to not be the ideal solution to explain the explosion of SN 1986G. There is no consistency between the $E_{\rm kin}$ implied by the density distribution (1.3×10^{51} erg) and that calculated using the abundance distribution (0.8×10^{51} erg).

It was found that a low energy W7 profile (W7e0.7) produced the best results. The fact that the W7e0.7 model yields a sensible abundance distribution and a consistent

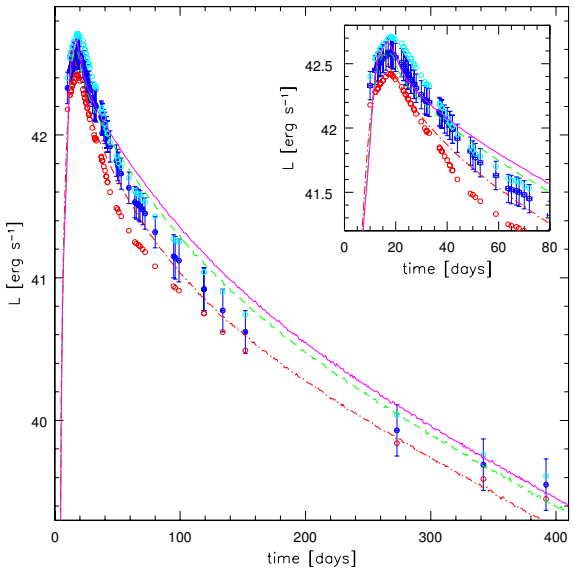

Figure 14. The observed (blue dots) bolometric light curve with the upper (cyan markers) and lower (red markers) limits. As well as the modelled LC using the derived abundance distribution from the W7 (green), Sub-Ch (red) and W7e0.7 (purple) density profiles.

model demonstrates that any deviation from this mass should be minor. The final integrated masses of the various elements that were obtained from the W7e0.7 model are: O+C=0.34 $M_\odot$, IME=0.69 $M_\odot$, stable NSE=0.21 $M_\odot$ and ^{56}Ni=0.14 $M_\odot$. These abundances produce a $E_{\rm kin}$ of 0.97×10^{51} erg, which is consistent with the energy of the W7e0.7 density profile (0.9×10^{51} erg).

In conclusion, SN 1986G is a low-energy Chandrasekhar mass explosion of a C+O WD, which produced a small amount of ^{56}Ni and a large amount of IMEs. The spectra of SN 1986G show signs of progenitor C II as late as -3 days from *B* band maximum. Although SN 1986G was a rapidly-declining SN Ia, we find no reason for it to deviate from a Chandrasekhar mass explosion. SN 1986G may be classified as the extreme end of the normal population of SNe Ia, rather than part of the sub-luminous population. It is even more peculiar in properties than SN 2004eo. However, like SN 2004eo its low luminosity can be interpreted as the explosion having a strong deflagration phase, which unbinds the expansion of the star, reducing the density and therefore the effectiveness of the successive supersonic burning phase. This led to the production of a large fraction of IMEs (Mazzali et al. 2008).

These findings raise the possibility that only SNe Ia with very large decline rates deviate from a Chandrasekhar mass. The uncertainties in the analysis lie in the value of host galaxy extinction and the gaps in spectral coverage. However, SN 1986G is the only SN Ia with properties falling in the gap between normal and subluminous SNe Ia that also has a good time-series of spectra. Thus our analysis of SN 1986G explores an important region in parameter space in the overall SNe Ia picture.

ACKNOWLEDGMENTS

Some of the data presented in this paper were obtained from the Mikulski Archive for Space Telescopes (MAST). STScI is operated by the Association of Universities for Research in Astronomy, Inc., under NASA contract NAS5-26555. Support for MAST for non-HST data is provided by the NASA Office of Space Science via grant NNX09AF08G and by other grants and contracts. We have used data from the NASA / IPAC Extragalactic Database (NED, http://nedwww.ipac.caltech.edu, operated by the Jet Propulsion Laboratory, C alifornia Institute of Technology, under contract with the National Aeronautics and Space Administration). For data handling, we have made use of various software (as mentioned in the text) including IRAF. IRAF Image Reduction and Analysis Facility (http://iraf.noao.edu) is an astronomical data reduction software distributed by the National Optical Astronomy Observatory (NOAO, operated by AURA, Inc., under contract with the National Science Foundation).

REFERENCES

Abbott D. C., Lucy L. B., 1985, ApJ, 288, 679
Anderson J. P., James P. A., Förster F., González-Gaitán S., Habergham S. M., Hamuy M., Lyman J. D., 2015, MNRAS, 448, 732
Ashall C., Mazzali P., Bersier D., Hachinger S., Phillips M., Percival S., James P., Maguire K., 2014, MNRAS, 445, 4427
Ashall C., Mazzali P., Sasdelli M., Prentice S. J., 2016, MNRAS, 460, 3529
Axelrod T. S., 1980, PhD thesis, California Univ., Santa Cruz.
Baade W., Minkowski R., 1954, ApJ, 119, 215
Bland J., Taylor K., Atherton P. D., 1987, MNRAS, 228, 595
Cappellaro E., Mazzali P. A., Benetti S., Danziger I. J., Turatto M., della Valle M., Patat F., 1997, A&A, 328, 203
Cardelli J. A., Clayton G. C., Mathis J. S., 1989, ApJ, 345, 245
Cristiani S., et al., 1992, A&A, 259, 63
Ferrarese L., Mould J. R., Stetson P. B., Tonry J. L., Blakeslee J. P., Ajhar E. A., 2007, ApJ, 654, 186
Foley R. J., et al., 2012, ApJ, 753, L5
Frogel J. A., Gregory B., Kawara K., Laney D., Phillips M. M., Terndrup D., Vrba F., Whitford A. E., 1987, ApJ, 315, L129
Fukugita M., Shimasaku K., Ichikawa T., 1995, PASP, 107, 945
Hachinger S., Mazzali P. A., Benetti S., 2006, MNRAS, 370, 299
Hachinger S., Mazzali P. A., Taubenberger S., Pakmor R., Hillebrandt W., 2009, MNRAS, 399, 1238
Hachinger S., Mazzali P. A., Sullivan 2013, MNRAS, 429, 2228
Höflich P., Gerardy C. L., Fesen R. A., Sakai S., 2002, ApJ, 568, 791
Iben Jr. I., Tutukov A. V., 1984, ApJS, 54, 335
Iwamoto K., Brachwitz F., Nomoto K., Kishimoto N., Umeda H., Hix W. R., Thielemann F.-K., 1999, ApJS, 125, 439
Leibundgut B., et al., 1993, AJ, 105, 301
Livne E., Arnett D., 1995, ApJ, 452, 62
Lucy L. B., 1999, A&A, 345, 211
Mazzali P. A., 2000, A&A, 363, 705
Mazzali P. A., Hachinger S., 2012, MNRAS, 424, 2926
Mazzali P. A., Lucy L. B., 1993, A&A, 279, 447
Mazzali P. A., Lucy L. B., Danziger I. J., Gouiffes C., Cappellaro E., Turatto M., 1993, A&A, 269, 423
Mazzali P. A., Cappellaro E., Danziger I. J., Turatto M., Benetti S., 1998, ApJ, 499, L49
Mazzali P. A., Nomoto K., Cappellaro E., Nakamura T., Umeda H., Iwamoto K., 2001, ApJ, 547, 988

Mazzali P. A., Röpke F. K., Benetti S., Hillebrandt W., 2007a, Science, 315, 825
Mazzali P. A., et al., 2007b, ApJ, 661, 892
Mazzali P. A., Sauer D. N., Pastorello A., Benetti S., Hillebrandt W., 2008, MNRAS, 386, 1897
Mazzali P. A., Maurer I., Stritzinger M., Taubenberger S., Benetti S., Hachinger S., 2011, MNRAS, 416, 881
Mazzali P. A., Sullivan M., Hachinger S., 2014, MNRAS, 439, 1959
Mazzali P. A., et al., 2015, MNRAS, 450, 2631
Munari U., Henden A., Belligoli R., Castellani F., Cherini G., Righetti G. L., Vagnozzi A., 2013, New Astron., 20, 30
Nomoto K., Thielemann F.-K., Yokoi K., 1984, ApJ, 286, 644
Nomoto K., Iwamoto K., Kishimoto N., 1997, Science, 276, 1378
Nugent P., Phillips M., Baron E., Branch D., Hauschildt P., 1995, ApJ, 455, L147
Pastorello A., Mazzali P. A., Pignata G., Benetti S., Cappellaro E., Filippenko A. V., Li W., 2007, MNRAS, 377, 1531
Pauldrach A. W. A., Duschinger M., Mazzali P. A., Puls J., Lennon M., Miller D. L., 1996, A&A, 312, 525
Phillips M. M., 1993, ApJ, 413, L105
Phillips M. M., et al., 1987, PASP, 99, 592
Phillips M. M., Wells L. A., Suntzeff N. B., Hamuy M., Leibundgut B., Kirshner R. P., Foltz C. B., 1992, AJ, 103, 1632
Phillips M. M., Lira P., Suntzeff N. B., Schommer R. A., Hamuy M., Maza J., 1999, AJ, 118, 1766
Richter O.-G., Huchtmeier W. K., 1984, A&A, 132, 253
Rosswog S., Kasen D., Guillochon J., Ramirez-Ruiz E., 2009, ApJ, 705, L128
Sasdelli M., Mazzali P. A., Pian E., Nomoto K., Hachinger S., Cappellaro E., Benetti S., 2014, MNRAS, 445, 711
Sasdelli M., Ishida E. E. O., Hillebrandt W., Ashall C., Mazzali P. A., Prentice S., 2016, MNRAS,
Schlafly E. F., Finkbeiner D. P., 2011, ApJ, 737, 103
Shigeyama T., Nomoto K., Yamaoka H., Thielemann F.-K., 1992, ApJ, 386, L13
Soria R., et al., 1996, ApJ, 465, 79
Stehle M., Mazzali P. A., Benetti S., HillebrandtW. 2005, MNRAS, 360, 1231
Tanaka M., Mazzali P. A., Stanishev V., Maurer I., Kerzendorf W. E., Nomoto K., 2011, MNRAS, 410, 1725
Taubenberger S., Hachinger S., Pignata G., Mazzali P. A., Contreras C., Valenti S., 2008, MNRAS, 385, 75
Tubbs A. D., 1980, ApJ, 241, 969
Woosley S. E., Kasen D., Blinnikov S., Sorokina E., 2007, ApJ, 662, 487
Yoon S.-C., Langer N., 2005, A&A, 435, 967
de Vaucouleurs G., 1980, ApJ, 240, L93